Deriving CME Density From Remote Sensing Data and Comparison to In-Situ Measurements

M. Temmer[1] , **L. Holzknecht[1]**, **M. Dumbović[2]** , **B. Vršnak[2]** , **N. Sachdeva[3]** , **S. G. Heinemann[1]** , **K. Dissauer[1,4]** , **C. Scolini[5,6]** , **E. Asvestari[1,7]** , **A. M. Veronig[1,8]** , and **S. J. Hofmeister[1]**

[1]Institute of Physics, University of Graz, Graz, Austria, [2]Hvar Observatory, Faculty of Geodesy, University of Zagreb, Zagreb, Croatia, [3]Department of Climate and Space Sciences and Engineering, University of Michigan, Ann Arbor, MI, USA, [4]NorthWest Research Associates, Boulder, CO, USA, [5]Centre for Mathematical Plasma Astrophysics (CmPA), Leuven, Belgium, [6]Solar-Terrestrial Centre for Excellence – SIDC, Royal Observatory of Belgium, Brussels, Belgium, [7]Department of Physics, University of Helsinki, Helsinki, Finland, [8]Kanzelhöhe Observatory for Solar and Environmental Research, University of Graz, Graz, Austria

Abstract We determine the three-dimensional geometry and deprojected mass of 29 well-observed coronal mass ejections (CMEs) and their interplanetary counterparts (ICMEs) using combined Solar Terrestrial Relations Observatory - Solar and Heliospheric Observatory white-light data. From the geometry parameters, we calculate the volume of the CME for the magnetic ejecta (flux-rope type geometry) and sheath structure (shell-like geometry resembling the (I)CME frontal rim). Working under the assumption that the CME mass is roughly equally distributed within a specific volume, we expand the CME self-similarly and calculate the CME density for distances close to the Sun (15–30 Rs) and at 1 AU. Specific trends are derived comparing calculated and in-situ measured proton densities at 1 AU, though large uncertainties are revealed due to the unknown mass and geometry evolution: (1) a moderate correlation for the magnetic structure having a mass that stays rather constant ($cc \approx 0.56 - 0.59$), and (2) a weak correlation for the sheath density ($cc \approx 0.26$) by assuming the sheath region is an extra mass—as expected for a mass pile-up process—that is in its amount comparable to the initial CME deprojected mass. High correlations are derived between in-situ measured sheath density and the solar wind density ($cc \approx -0.73$) and solar wind speed ($cc \approx 0.56$) as measured 24 h ahead of the arrival of the disturbance. This gives additional confirmation that the sheath-plasma indeed stems from piled-up solar wind material. While the CME interplanetary propagation speed is not related to the sheath density, the size of the CME may play some role in how much material could be piled up.

1. Introduction

The propagation behavior of coronal mass ejections (CMEs) is governed by different forces at different heliocentric distances. Close to the Sun the propelling Lorentz force dominates, which is reinforced by magnetic reconnection processes (see Chen, 1989, 1996; Kliem & Török, 2006; Vršnak, 2008, 2016). With time, as the CME moves farther away from the Sun and the magnetic reconnection weakens, CME propagation is predominantly governed by its interaction with the ambient solar wind flow (see e.g., Cargill et al., 1996; Sachdeva et al., 2015; Temmer et al., 2011; Vršnak, 2001; Vršnak et al., 2013). The magnetohydrodynamic CME drag can be expressed analogously to the aerodynamic drag. It is dependent on the CME geometry, that is, cross-section and width, density and speed relative to the ambient solar wind (see e.g., Vršnak et al., 2010). The ram-pressure defined by the CME impact speed and density, is found to be well correlated to the amplitude of sudden storm commencements caused by the rapid compression of the Earth's magnetic field (Gonzalez et al., 1989). Methods for deriving the CME speed and arrival time at Earth from the CME initial speed close to the Sun have been largely tested (e.g., Dumbovic et al., 2018; Mays et al., 2015; Riley et al., 2018; Sachdeva et al., 2015; Vršnak et al., 2013). However, the derivation of the CME density using remote sensing data and its evolution to 1 AU has not been investigated yet.

In-situ measurements of the interplanetary counterpart of CMEs (ICMEs; note that we follow the notation by Rouillard (2011) and use the term ICME such to include the shock signature, the sheath and the magnetic structure of the CME) at 1 AU reveal that the density of the sheath region is larger compared to the

density within the magnetic ejecta region (e.g., see Masías-Meza et al., 2016). This can be well explained by the expansion of the low plasma beta magnetic structure that dilutes the plasma material ejected from the Sun. As the CME propagates and expands, solar wind material piles-up in front of the driver forming the sheath region as was reproduced by Magnetohydrodynamics simulations (e.g., Siscoe & Odstrcil, 2008). ICME sheath regions reveal in general different characteristics compared to the magnetic ejecta regions. In particular, they show low alpha to proton and Fe/O ratios, characteristic of the ambient solar wind, and stronger turbulence (e.g., see Kilpua et al., 2017; Owens, 2018). Evidence that the sheath becomes more prominent in interplanetary space is also given by a relative increase of the sheath durations from Mercury to Earth (Janvier et al., 2019). Recent studies using remote sensing data suggest that in the early CME evolution, there is no significant mass pile-up ahead of the CME (Howard & Vourlidas, 2018). Observed mass increases up to 20 solar radii (R_s) which is most probably due to outflows from the solar surface (Bein et al., 2013; Bemporad & Mancuso, 2010; Temmer et al., 2017; Veronig et al., 2019).

A changing CME mass has consequences for the drag force acting on the CME in interplanetary space (Cargill, 2004; Vršnak et al., 2008), and with that modifies the CME propagation time, impact speed, and energy input to the magnetosphere (Takahashi & Shibata, 2017). Moreover, a better understanding and quantification of CME mass density close to the Sun is important to provide accurate inputs for numerical models in order to properly simulate CME propagation and to predict Space Weather. Usually the CME mass density is taken as a constant default value based on observational studies of streamer densities. For example, ENLIL (Odstrčil & Pizzo, 1999) uses the so-called CME cloud density (dcld) parameter that by default is four times larger than typical mean values in the ambient fast wind (see Mays et al., 2015), and for EUHFORIA (Pomoell & Poedts, 2018), a value of 10^{-18} kg/m^3 is taken corresponding to dcld = 2, that is, half of the density used by default in ENLIL (dcld = 4).

With the launch of the Solar Terrestrial Relations Observatory (STEREO; Kaiser et al., 2008) and its SECCHI instrument suite (Howard et al., 2008) in 2006, the interplanetary evolution of the CME structure in white-light can be measured seamlessly over the Sun-Earth distance range and is used to derive the CME kinematics all the way from Sun to 1 AU. Tracking density and mass from Sun to Earth is a quite complex undertaking. In a case study, Savani et al. (2013) showed a qualitative comparison of an estimated mass profile for the sheath structure using white-light heliospheric image data that resembled quite well the in-situ density measurements. In the current study, we aim for a better understanding of the density evolution of the ICME sheath and magnetic structure. Furthermore, we derive the CME density close to the Sun in order to feed CME propagation models. For a set of 29 well-observed multi-viewpoint STEREO CME-ICME pairs, we perform a statistical study covering the derivation of the CME kinematics, deprojected mass, and three-dimensional geometry parameters from which we calculate the CME volume and density, and compare the results to in-situ measurements at 1 AU.

The paper is structured as follows. In Section 2, the data set and the methodology are presented. Section 3 gives the analysis and results. In Sections 4 and 5, the results are discussed and summarized. In the Appendix, we provide for all studied events physical parameters that can be used as input for CME propagation models.

2. Data and Methods

The study is based on a sample of 29 well-observed CME-ICME pairs that occurred in the period December 2008–August 2014 (extracted parameters for each event are given in the Appendix in Table A1). The events were selected so as to have reliable stereoscopic observations plus a spacecraft encounter from which we derive clear in-situ plasma and magnetic field measurements. In that respect, we restricted our selection to CMEs that were observed by both STEREO satellites (Ahead and Behind) and revealed in-situ signatures at L1 by Wind. To correctly link the CME-ICME pairs we first estimated the CME arrival time at 1 AU using the drag-based model by Vršnak et al. (2013) (available as ESA tool under: http://swe.ssa.esa.int/web/guest/graz-dbm-federated) with the CME initial speed, distance, and angular extent in the ecliptic plane as obtained from the graduated cylindrical shell (GCS) reconstruction (see also Dumbović et al., 2019). Applying a time window of ±18 h, centered at the calculated arrival time, we searched in the in-situ data for the corresponding ICME characteristics. All the results are cross-checked with ready lists from Richardson
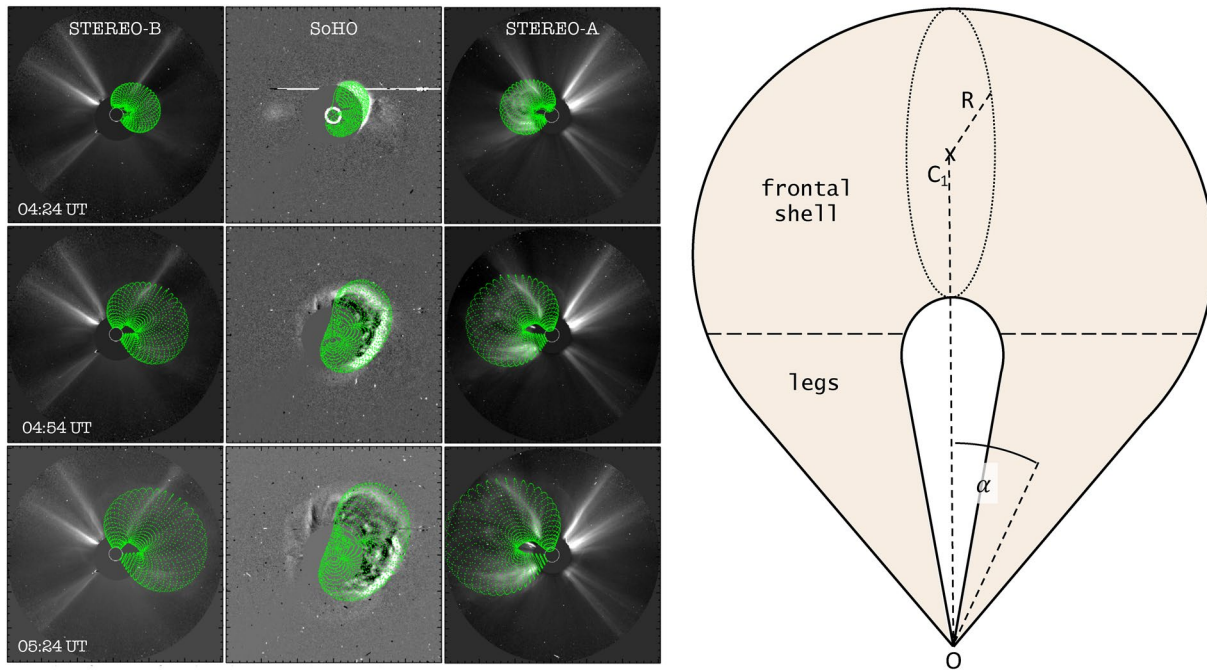
Figure 1. Left: Example of the three-dimensional geometry for the CME from 4 August 2011 reconstructed using the GCS model by Thernisien (2011) for three vantage points (COR2 from STEREO-A and -B, and LASCO/C3). Right: Sketch of the GCS model giving the parameters required for calculating the CME volume (α is the angular half-width, C_1 is the apex center, R is the cross-section radius at the apex). GCS "full volume", as given in the text, refers to the frontal shell plus legs.

and Cane (2010, to which we refer further on as R&C list), Wood et al. (2017), and HELCATS (Heliospheric Cataloging, Analysis and Techniques Service) WP4 catalog (LINKCAT).

For the linked CME-ICME events verified in this way, we obtain from stereoscopic observations their three-dimensional parameters close to the Sun such as propagation direction, speed, geometry, and furthermore the deprojected mass (see Colaninno & Vourlidas, 2009) and in situ characteristics for near-Earth space. The geometry and volume of a CME together with its deprojected mass is further used to estimate the particle density of an ICME at 1 AU applying to the CME volume a self-similar expansion with different expansion rates. For comparing calculated and measured in-situ densities as well as other parameters, we use the bootstrap method. We apply 10^4 repetitions, that is, the bootstrapping procedure re-samples the original data 10,000 times from which 10,000 statistical samples are created in order to derive the Spearman median correlation coefficient and an 80% empirical confidence interval (Efron, 1979; Efron & Tibshirani, 1993).

2.1. Parameter Definition Close to the Sun

The CME three-dimensional geometry at a distance range of about 15 R_s is reconstructed with the GCS model (see Thernisien et al., 2009; Thernisien, 2011) using combined white-light coronagraph data from 2 or 3 different viewpoints of SECCHI/COR2 aboard STEREO-A and -B and LASCO/C2/C3 aboard the Solar and Heliospheric Observatory (SOHO; Domingo et al., 1995). The GCS model represents an idealized geometry of a CME flux rope as a hollow croissant-shaped mesh that is manually fitted to white-light data with the presumed magnetic structure of the CME. The left panels in Figure 1 show a GCS reconstructed flux rope for the CME event on 4 August 2011 covering the height range 8–16 R_s at three time steps. As this reconstruction is subjective, we aim to avoid bias and use for the study GCS reconstructions performed independently by three different groups: (a) N. Sachdeva thesis (Sachdeva, 2019), 12 events using three s/c viewpoints; (b) UNIGRAZ, 10 events using three s/c viewpoints; (c) HELCATS WP3 COR2 Catalogue KIN-CAT (which builds on the work undertaken during the EU FP7 AFFECTS project), seven events using two s/c viewpoints from STEREO-A and -B.
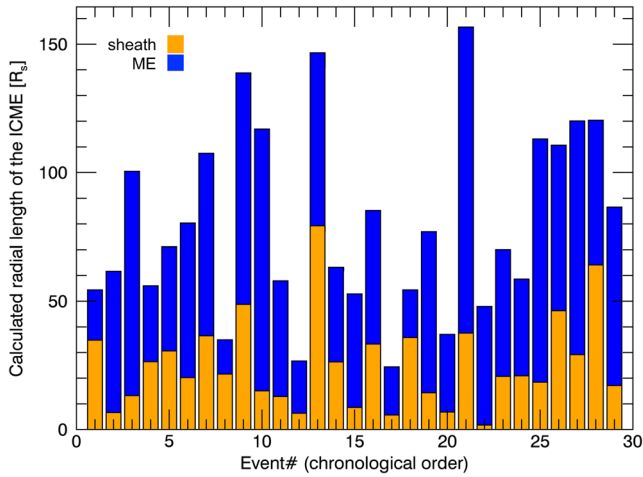
Figure 2. Radial size of interplanetary coronal mass ejections (ICME) structures (sheath and magnetic ejecta [ME]) at 1 AU for each event that is used for the volume calculation. As reference point the shock arrival time is used which is set to $h = 215$ R$_s$. Sheath is given in orange, ME in blue.

The CME volume (V) is calculated as function of height/distance using the GCS parameters α (angular half-width) and κ (aspect ratio) as described in Holzknecht et al. (2018). The right panel of Figure 1 sketches the derivation of those parameters with $\alpha, \kappa = (\overline{OC_1}) / R$ (where O is the center of the Sun, C_1 is the apex center, and R is the cross-section radius at apex), and h is the height of the leading edge given as $h = (\overline{OC_1}) + R$ according to Thernisien (2011). The entire GCS volume consists of the frontal shell and two legs. Over the LASCO field of view up to $h = 30$ R$_s$, a self-similar expansion is assumed. From this, we define the full volume of the expanding GCS flux rope, V_{fr}, close to the Sun.

The CME deprojected mass in the corona, m_{dp}, is derived at ~15 R$_s$ by using combined white-light coronagraph data from SECCHI/COR2 aboard STEREO-A and -B. The method assumes that the difference in the white-light excess brightness, as measured by the two STEREO spacecraft, is due to the plane of sky projection of an optically thin source. The brightness excess is converted into electron excess, hence, mass, assuming a composition of 90% hydrogen and 10% helium. The masses calculated from the two vantage points are then corrected for the CME propagation direction. This is done by varying consistently the masses derived from each vantage point until they yield the same result. The technique and application is described in Colaninno and Vourlidas (2009) and Bein et al. (2013). The region of interest from which the mass is derived, was defined either manually by drawing the flux rope boundary or, as given for the HELCATS catalog, by using the GCS model boundaries (Pluta et al., 2019; Savani et al., 2013). A cross-check between both approaches revealed no systematic differences in the derived mass.

2.2. Parameter Definition for Near-Earth Space

In-situ plasma and interplanetary magnetic field measurements (5-min averaged) are taken from the Wind spacecraft and its Solar Wind Experiment (Ogilvie et al., 1995) and Magnetic Field Experiment (Lepping et al., 1995). We extract from the R&C list the times of the shock arrival and start/end times of the magnetic ejecta (ME) structure (based primarily on plasma and magnetic field observations; for more details, see Richardson & Cane, 2010) from which we define the sheath and ME region. In this study we primarily use the arithmetic mean and standard deviation of in-situ measured plasma density and speed, over the duration of each structure (see Appendix A for additional parameters that were extracted).

As the CME expands in interplanetary space, it propagates over the spacecraft with the sheath region being detected first, followed by the ME. Figure 2 gives the radial size of the sheath and ME structure for each of the events. They are calculated by multiplying the duration of the sheath (shock arrival time until start time of ME) and duration of the ME (start time of ME until end time of ME), respectively, by the average speed of each structure (we note that this method assumes constant expansion over the averaging time interval). The sheath is of shorter duration/size compared to the ME, hence relates also to a smaller volume. For calculating densities of the ME and sheath structure we use therefore different volumes. Figure 3 sketches the CME volume derivation using the in-situ measurements of an ICME at 1 AU. The arrival time of the ICME shock is used as reference point and sets h to 215 R$_s$ (average 1 AU distance). The derived distances are used for calculating the full CME volume (frontal shell plus legs; cf., right panel of Figure 1) for the sheath and ME structure. We define (1) V_{215} as the volume up to the in-situ measured shock by expanding the GCS flux rope to $h = 215$ R$_s$, (2) V_{sh} as the sheath volume by expanding the GCS flux rope to $h = 215$ R$_s$ + sheath distance, and (3) V_{ME} as the ME volume by expanding the GCS flux rope to $h = 215$ R$_s$ + sheath distance + ME distance.

For calculating the densities from the volume and mass, we assume that (1) the observed initial deprojected mass from white-light data represents mostly plasma within the ME volume, $m_{ME} \approx m_{dp}$; (2) the mass is uniformly distributed within the volume structures; (3) the ME structure may have some mass exchange with
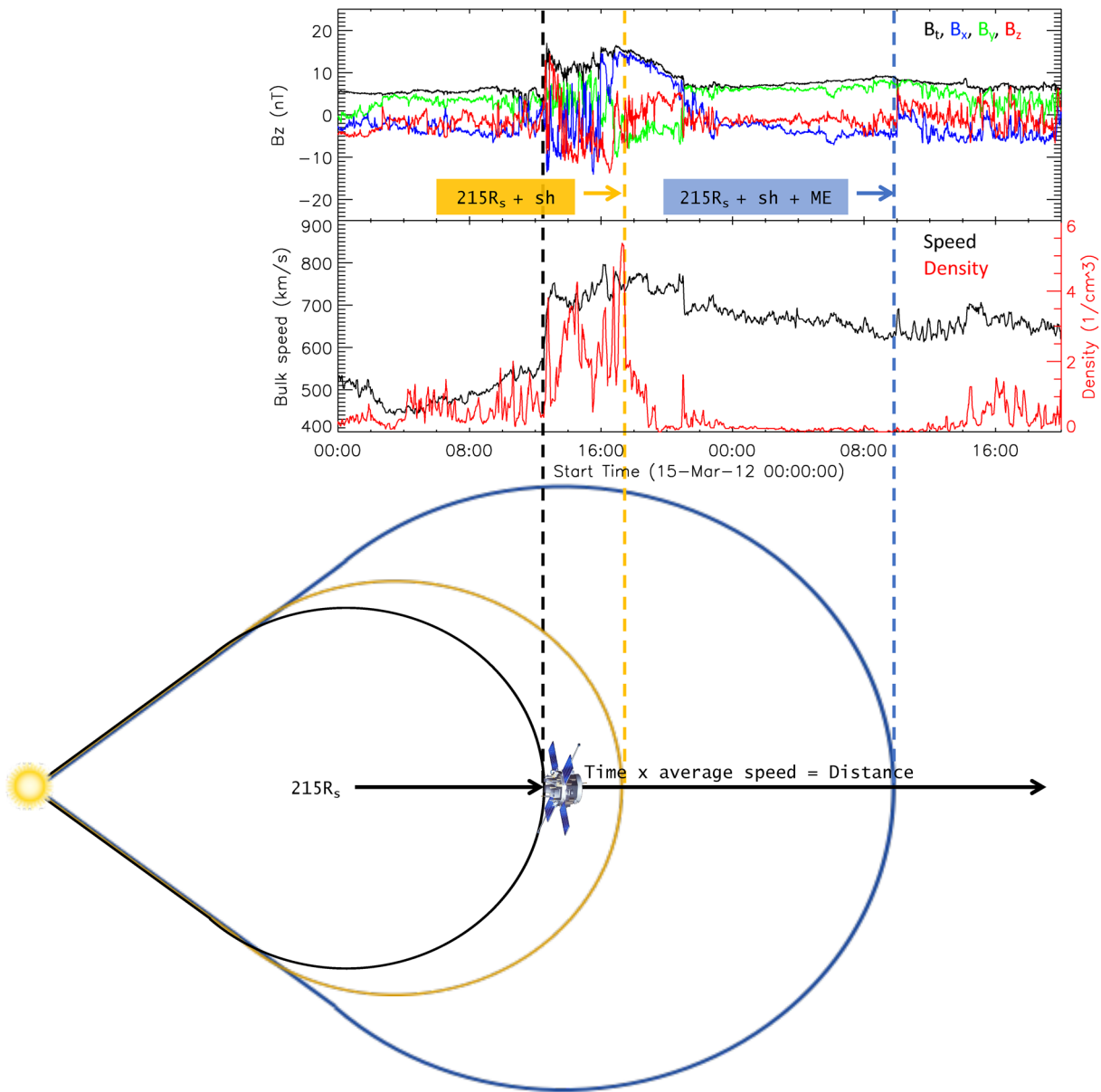
Figure 3. Sketch of volume calculation in relation to the in-situ measured ICME structures (sheath, ME). Different radial sizes of the GCS geometries are used for the volume calculation. Black: V_{215} derived from a radial size of 215 R_s; orange: V_{sh} derived from the radial size 215 R_s + sheath; blue: V_{ME} is derived from the radial size 215 R_s + sheath + ME.

the interplanetary medium, that is, the ME experiences either mass loss due to erosion or mass growth due to reconnection with the interplanetary magnetic field (see e.g., Dasso et al., 2007; Manchester et al., 2014; Ruffenach et al., 2015); (4) the sheath region acquires additional mass, due to mass accumulation at the CME front while propagating in interplanetary space. DeForest et al. (2013) found from an observational case study a CME mass increase by 60%, that would be consistent with swept up solar wind material in the sheath region. According to these assumptions we vary the mass of the ME structure and the sheath region. The mass of the ME structure, m_{ME}, is varied by ±25% of the initial deprojected mass m_{dp}. The sheath region mass, m_{sh}, is calculated for 0.5, 1, and 1.5 times m_{dp}. The entire CME mass at 1 AU yields $m_{total} = m_{ME} + m_{sh}$. For the volume, we consider self-similar expansion with different expansion trends by varying the expansion factor x when calculating the flux rope radius with $R(h) = R_0(h / h_0)^x$, where R_0 and h_0 refer to the starting value at $h = 15$ R_s. Different expansion rates are tested by varying x in the range of 0.8–1.1 (in steps of 0.1) according to results from observational studies (e.g., Bothmer & Schwenn, 1998; Démoulin et al., 2008;
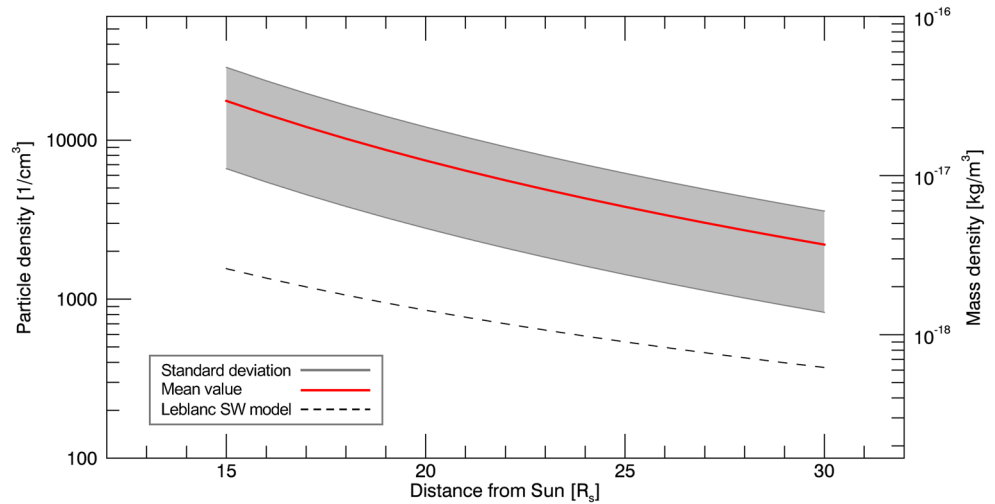
Figure 4. CME density over the distance range 15–30 R_s. We assume that the coronal mass ejections (CME) flux rope (full volume) expands in a self-similar manner ($x = 1.0$) and derive for all 29 events the mean distance-density profile (red line) together with its standard deviations (black lines), as calculated from α, κ and $m_{ME} = m_{dp}$ values for the individual events. As comparison, we give the density profile from the empirical solar wind model by Leblanc et al. (1998) with the density at 1 AU normalized to $n_p = 7$ cm^{-3} (dashed line).

Gulisano et al., 2012; Leitner et al., 2007; Vršnak et al., 2019). For comparison with in-situ data, we derive the proton number density, n_p, given in cm^{-3} by assuming abundances of 90% hydrogen and 10% helium.

3. Results

3.1. CME Density Profile for 15–30 R_s

Close to the Sun, for the distance range up to 30 R_s from observational studies no mass pile-up is reported (Howard & Vourlidas, 2018). Assuming that the estimated deprojected mass represents mostly plasma within the ME volume, Figure 4 shows for the entire sample of 29 events the average CME density profile, ρ (h), and standard deviation over the distance range $h = 15 - 30$ R_s derived by $\rho\,(h) = m_{dp}/V_{fr}\,(h)$ and assuming self-similar expansion ($x = 1$) and a uniform plasma distribution within the CME structure. The plot presents the CME proton number density, n_p, in particles per cm^3 (left y-axis) and the corresponding mass density in kg m^{-3} (right y-axis). On average, over the distance range 15–30 R_s the CME particle density lies in the range of $\sim (2.2 - 17.6) \times 10^3$ cm^{-3} (mass densities with $\sim (3.6 - 29) \times 10^{-18}$ kg m^{-3}). For comparison, we give the solar wind density profile applying the relation by Leblanc et al. (1998). From this we derive a ratio between CME and solar wind density that decreases from $\sim$11 at $h = 15$ R_s to $\sim$6 at $h = 30$ R_s.

3.2. Comparing Calculated and In-Situ Measured Densities Using the Full Volume

Figure 5 gives the comparison between calculated (x-axis) and measured (y-axis) proton plasma densities at 1 AU, separately for the sheath and ME structure. For the volume derivation of the sheath (V_{sh}) and ME (V_{ME}) we vary the expansion factor in the range $x = 0.8$–1.1. The results are derived in a first approximation by simply applying a mass of $m_{sh} = m_{ME} = m_{dp}$. For low expansion factors, $x = 0.8$–0.9, the calculated plasma densities are obtained to be of the same order of magnitude as the in-situ measured ones. These findings first of all support that the CME geometry/volume derivation and mass calculation based on remote sensing image data are physically meaningful. The sheath region does not consist of coronal CME plasma, but likely piled-up preceding solar wind plasma. Therefore, the sheath region has to be considered as an extra mass separate to the coronal CME mass (cf. Kilpua et al., 2017). For larger volumes using $x = 1.0$–1.1, the calculated densities tend to get underestimated.

In a next step, we vary the mass of the different structures for taking into account evolutionary process-es, just like erosion or mass accumulation in interplanetary space. Figure 6 shows the derived differences
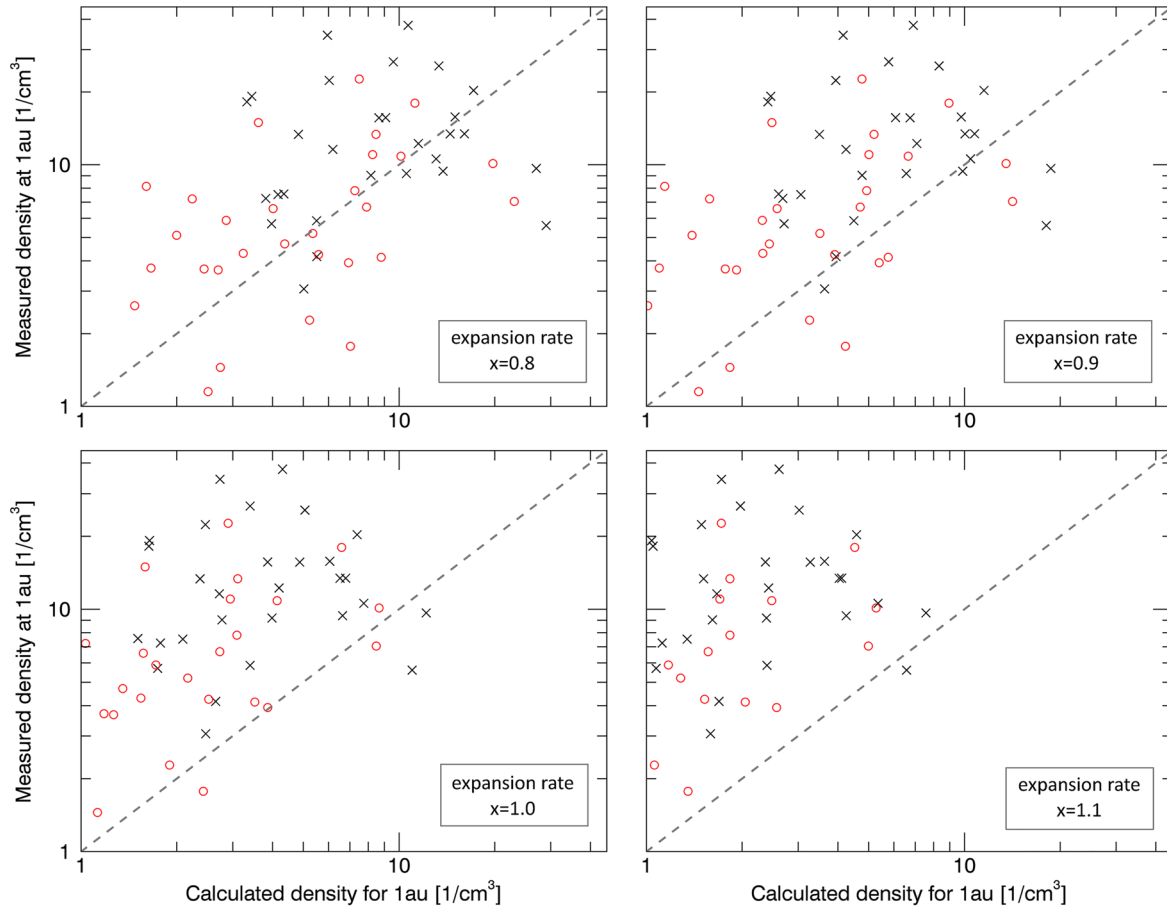
Figure 5. Log-log plot of the calculated versus measured particle density using the full volume for each structure and different expansion factors (see legend). Magnetic ejecta (ME) is marked by red circles, sheath by black crosses. Gray dashed line gives the $x = y$ equality. The used input mass is $m_{\mathrm{sh}} = m_{\mathrm{ME}} = m_{\mathrm{dp}}$.

between the calculated and observed plasma densities using different expansion factors and input mass, represented as box and whiskers plot containing the minimum, lower quartile, median, upper quartile, and maximum for each value array. Table 1 (two left columns) gives the median values and standard deviation for the derived differences between the calculated and measured plasma density values. In general, the calculated plasma densities tend to be underestimated when compared with in-situ measurements. This effect increases for larger volume expansions ($x > 0.9$). For the sheath region, using 50% of the initial deprojected mass the results are not satisfying. However, when increasing the mass to $1.5 \times m_{\mathrm{dp}}$ and using $x = 0.8$, the results improve showing differences between calculated and measured densities that are distributed around zero. For the ME region, mass inputs of $0.75 - 1.25 \times m_{\mathrm{dp}}$ result in a fair match with the observations with best results for a constant mass or increased mass and low volume expansion ($x = 0.8$–0.9). Table 2 (two left columns) summarizes the resulting Spearman median correlation coefficients and 80% confidence intervals from the bootstrapping method separately for sheath and ME structure applying different expansion factors. We note that different mass inputs do not affect the rank-order correlation coefficient. We find that the correlations between measured and calculated particle densities for each structure at 1 AU differ strongly. While the ME region shows a weak correlation ($cc \approx 0.47 - 0.49$) though with large spread, for the sheath region almost no correlation is found ($cc \approx 0.11 - 0.19$).

3.3. Comparing Calculated and In Situ Measured Densities Using a Reduced Volume

The ME seems rather well reproduced with the simple GCS flux rope geometry. We also find that lower expansion factors tend to give better results in terms of more symmetrically distributed values around the line of equality between calculated and measured densities. So far, in our simple approach, we have assumed
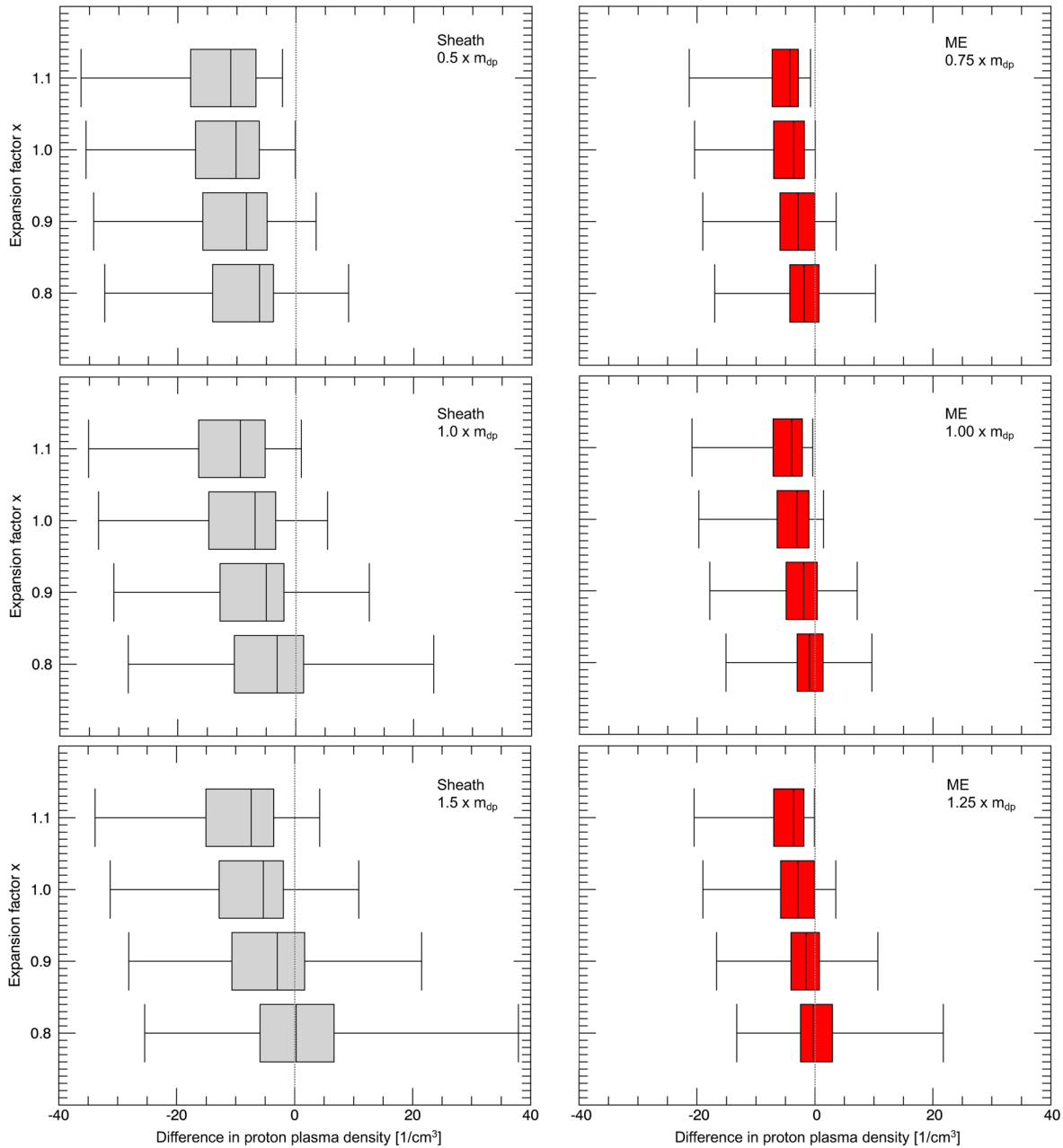
Figure 6. Boxplot showing the differences between calculated and observed proton plasma density (left panel sheath; right panel ME region) using different expansion factors. Different multiples of the derived deprojected mass (see plot legends) are used to calculate from the full volume the proton plasma density separately for the sheath and ME region. The whiskers give the minimum and maximum values, and the box itself is confined by the lower and upper quartile, with the vertical line within marking the median.

that the plasma of the sheath region is distributed within a flux-rope type geometry, same as the ME but of smaller volume. However, the sheath region presumably has not a flux-rope type but more likely a shell-like geometry. For improving the statistics we test various geometries for the volume derivations (e.g., subtracting differently expanding volumes from each other) and find best results for a "reduced volume" which is sketched in Figure 7. First, the sheath volume is based solely on the frontal shell geometry of the GCS reconstructed flux rope (see also Figure 1), while for the ME the basis is still the entire GCS flux rope. Then from both structures corresponding volumes for $h = 215$ R_s are subtracted (cf., Figure 7), meaning that we calculate the reduced volumes by $V_{ME,red} = V_{ME} - V_{215}$ and $V_{sh,red} = V_{ME,frontal} - V_{215,frontal}$.

Table 1
Median Values and Standard Deviation for the Derived Differences Between Measured and Calculated Density Values (see Figures 6 and 8)

		Full volume		Reduced volume	
x	m_x	Sheath	ME	Sheath	ME
0.8	a	−6.2 ± 9.3	−1.9 ± 5.2	−5.3 ± 15.6	+1.1 ± 11.1
0.8	b	−3.1 ± 10.9	−1.0 ± 5.8	−1.2 ± 26.8	+2.0 ± 14.8
0.8	c	+ 0.3 ± 13.2	−0.3 ± 6.6	+ 5.0 ± 38.7	+4.4 ± 18.6
0.9	a	−8.4 ± 9.0	−2.9 ± 4.8	−8.3 ± 11.3	−1.1 ± 6.9
0.9	b	−5.0 ± 9.8	−2.0 ± 4.9	−5.1 ± 16.4	−0.3 ± 8.9
0.9	c	−2.9 ± 11.0	−1.5 ± 5.2	−2.9 ± 22.4	+1.0 ± 11.1
1.0	a	−10.1 ± 8.8	−3.6 ± 4.7	−10.6 ± 9.6	−2.9 ± 5.0
1.0	b	−6.9 ± 9.2	−3.1 ± 4.7	−8.1 ± 11.7	−1.8 ± 5.8
1.0	c	−5.3 ± 9.8	−2.9 ± 4.7	−5.9 ± 14.3	−0.9 ± 6.8
1.1	a	−11.0 ± 8.8	−4.2 ± 4.8	−11.4 ± 9.0	−3.7 ± 4.5
1.1	b	−9.4 ± 8.9	−4.0 ± 4.7	−10.5 ± 9.8	−3.3 ± 4.6
1.1	c	−7.4 ± 9.2	−3.6 ± 4.6	−9.2 ± 10.8	−3.1 ± 4.9

Notes. Different expansion rates x and volumes (full or reduced) were used for the sheath and magnetic ejecta (ME) region. The mass indices, m_x, refer to (1) $m_{sh} = 0.5 \times m_{dp}$ and $m_{ME} = 0.75 \times m_{dp}$; (2) $m_{sh} = 1.0 \times m_{dp}$ and $m_{ME} = 1.0 \times m_{dp}$; (3) $m_{sh} = 1.5 \times m_{dp}$ and $m_{ME} = 1.25 \times m_{dp}$.

Table 2
Spearman Median Correlation Coefficients (cc) and 80% Confidence Interval (CI 80%) Resulting From the Bootstrapping Analysis (See Figures 6 and 8)

	Full volume		Reduced volume	
x	Sheath	ME	Sheath	ME
0.8	0.19	0.47	0.25	0.56
(CI 80%)	(0.42; −0.07)	(0.64; 0.26)	(0.47; 0.01)	(0.71; 0.36)
0.9	0.14	0.47	0.25	0.57
(CI 80%)	(0.38; −0.11)	(0.63; 0.26)	(0.48; 0.01)	(0.71; 0.38)
1.0	0.14	0.48	0.26	0.58
(CI 80%)	(0.37; −0.11)	(0.65; 0.28)	(0.48; 0.01)	(0.72; 0.39)
1.1	0.11	0.49	0.26	0.59
(CI 80%)	(0.35; −0.13)	(0.65; 0.28)	(0.48; 0.01)	(0.73; 0.41)

Note. Different expansion rates x, and volumes (full or reduced) were used for the sheath and magnetic ejecta (ME) region. For more details see text.

In general, by applying the reduced volumes, some events yield calculated densities that largely exceed the measurements (maximum is ∼38 particles cm^{-3}). These are three events where we used $x = 0.8$ (in-situ shock arrival times: 11-April-10 13:04UT, 04-Feb-11 01:55UT, 17-Jun-11 02:41UT) and two events with $x = 0.9$ (in-situ shock arrival times: 04-Feb-11 01:55UT and 17-Jun-11 02:41UT). Figure 8 shows the differences between calculated and observed plasma densities, represented as box and whiskers plots (containing the minimum, lower quartile, median, upper quartile, and maximum for each value array). Table 1 (two right columns) gives the median and standard deviation for the derived differences between calculated and measured plasma density values. In comparison to the results for the full volume (Figure 6), the derived median values for sheath and ME are closer to zero, however, the spread in the values increases. For the ME structure the lower and upper quartile get narrower, while for the sheath region they increase. Best results for the sheath region are obtained for an extra mass which is comparable to the initial deprojected mass and for a CME geometry of weak expansion ($x = 0.8$). For the ME region, equally good results are obtained for either a decreased or constant mass and low expansion ($0.75 − 1.0 \times m_{dp}$; $x = 0.9$) or increased mass ($1.25 \times m_{dp}$) and a volume that is expanding with $x = 1.0$. The two right columns in Table 2 give for the reduced volume the Spearman median correlation coefficients between calculated and measured densities and 80% confidence intervals from the bootstrapping method separately for sheath and ME structure for the different expansion factors. For the sheath region, by applying a reduced volume, we obtain a slightly improved correlation with $cc \approx 0.26$ and for the ME structure we get $cc \approx 0.56–0.59$.

In order, to obtain more conclusive results about the interplay between ambient solar wind, CME characteristics and mass/density evolution, we further investigate the relation between observational parameters derived from remote sensing and in-situ data. Figure 9 shows the relation between measured density in the sheath and ME region versus solar wind plasma characteristics measured 24 h before the arrival of the disturbance (pre-event density and pre-event speed). In addition, we color-code each parameter pair with the CME transit time (time difference between CME LASCO/C2 first appearance and ICME shock arrival at 1 AU, given in hours). In contrast to 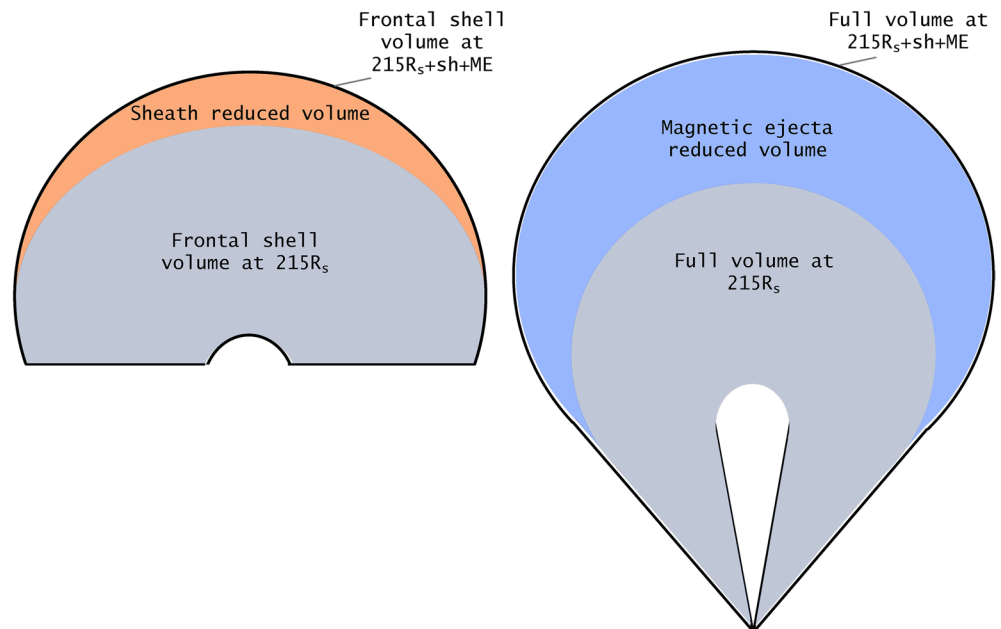the ME region, the sheath structure shows a much stronger dependence on the conditions ahead of the disturbance. The highest anti-correlation is found between sheath density and pre-event speed with $cc = −0.73$, and the largest positive correlation between sheath-density and pre-event density with $cc = 0.56$ (ME density and pre-event speed: $cc = −0.30$; ME density and pre-event density: $cc = 0.09$). Table 3 summarizes the Spearman median correlation coefficients and 80% confidence intervals from the bootstrapping method between the ICME sheath and ME density against solar wind plasma parameters (density and speed) and the total magnetic field, measured between 24 and 48 h before the arrival of the disturbance. The dependencies clearly decrease when relating the parameters to the conditions 48 h ahead of the disturbance. We find no dependencies on the CME transit time, hence, interplanetary CME speed, and no correlation to the pre-event magnetic field.

We further inspect how the size of the CME is related to the amount of piled-up solar wind material and other CME characteristics that are important for investigating the drag force in interplanetary space. Table 4 gives the statistical results from the bootstrapping analysis between the CME geometry parameters α (angular half-width) and κ (aspect ratio) as derived from GCS (as defined in Section 2.1) versus CME deprojected

Figure 7. Sketch of reduced volume derivation for the sheath region (left) and the ME region (right) that is derived by subtracting the CME volume up to $215R_s$.

mass, transit time, and in-situ measured particle densities for the sheath and ME region. We find a moderate anti-correlation between geometry and transit time ($cc = -0.60$ for α and $cc = -0.62$ for κ), while for the deprojected mass a moderate correlation with α ($cc = 0.67$) and a weak correlation with κ is obtained ($cc = 0.39$). Comparing the geometry parameters with in-situ measurements we get a weak to moderate correlation between α and κ, and the sheath density ($cc = 0.19$ and 0.30) and a very weak one for the ME density ($cc = -0.13$ and 0.16). Opposite to the ME, the sheath formation seems to be related to the CME size.

4. Discussion

The CME mass/density is a parameter that directly connects to the CME propagation behavior in interplanetary space. CMEs of high density will be less affected by the drag from the ambient solar medium compared to less dense ones. With that, the mass evolution of a CME in interplanetary space influences strongly the propagation duration and speed. Using for a sample of 29 CME-ICME pairs observational data from combined remote sensing and in-situ measurements together with geometry modeling efforts, we assess the CME mass/density evolution from Sun to Earth.

The geometry and volume of a CME together with its mass is derived from stereoscopic remote sensing data covering a field of view up to ~15 R_s. This is further used to estimate the particle density of an ICME at 1 AU applying a self-similar CME volume expansion with different expansion rates ($x = 0.8$–1.1). We treat the sheath region as extra mass (as first approach we simply use the same amount as the initial mass) and keep the ME initial mass and sheath mass constant as the CME expands. With that we find for $x = 0.8$–0.9 a rather good agreement between the ICME calculated and in-situ measured ME density. This supports that the available techniques are reasonable and adequate for deriving mass and volume by using remote sensing image data.

We show a novel approach for computing the CME density by applying GCS reconstruction for CMEs. By calculating the CME volume and expansion in interplanetary space, together with the deprojected mass, the density is derived for various distances from the Sun. As the obtained parameters are based on simplistic geometric modeling of a flux-rope-type CME, it is not surprising that the differences between calculated and observed densities are large. Nevertheless, the statistical results yield trends that allow to draw some conclusions. We derive a moderate relationship between calculated and in-situ measured densities with $cc = 0.47$–0.49 using a full volume and $cc = 0.56$–0.59 for a reduced volume. This finding may indicate that
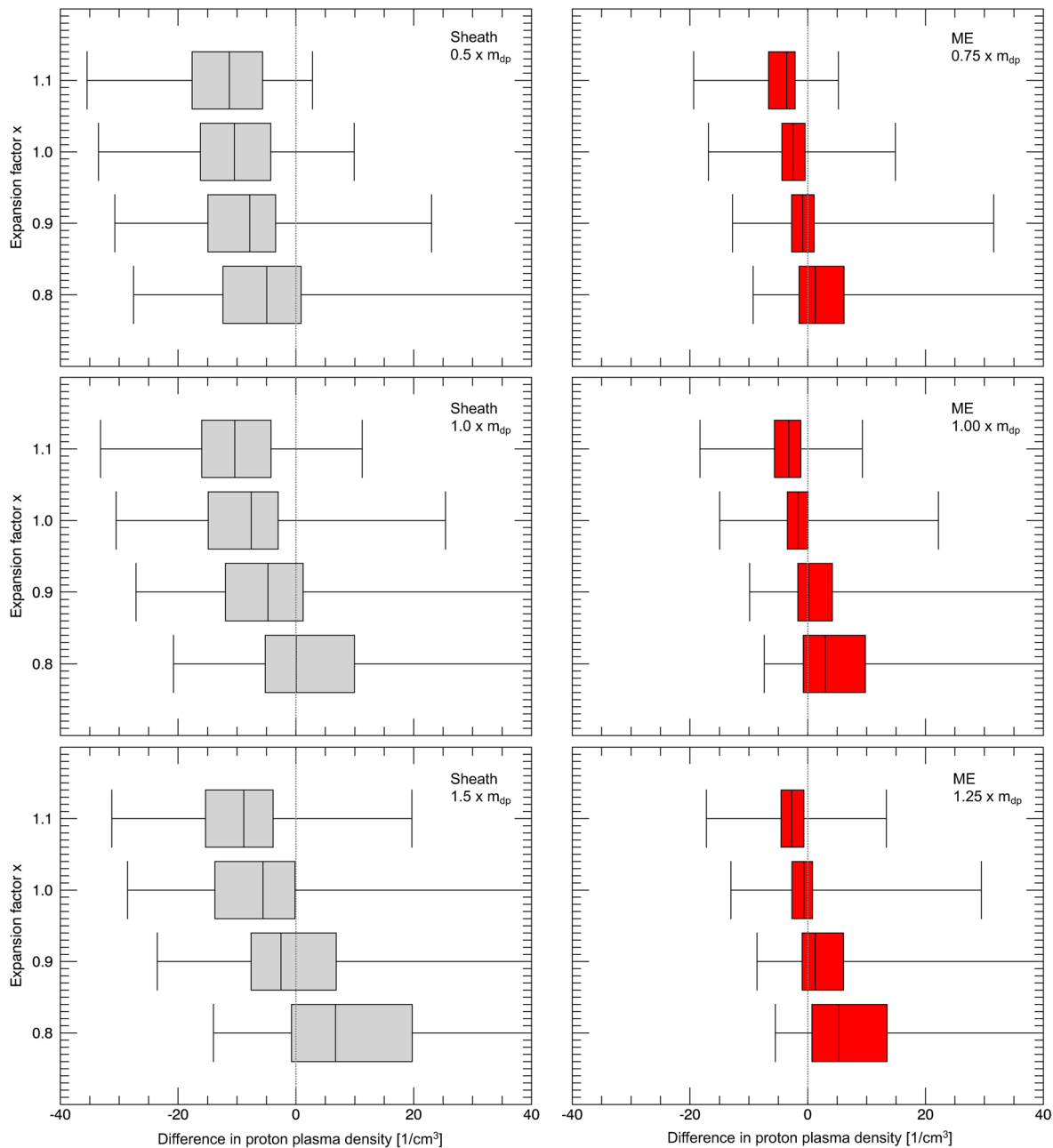
Figure 8. Same as Figure 6 but using the reduced volume for the calculation of sheath and ME plasma density.

the ME structure might be reproduced by a flux rope-like geometry. Statistically, the smallest differences between calculated and observed ME densities are derived for a low expansion factor and rather constant mass. This hints toward that the majority of the mass expelled from the Sun lies within the CME flux rope structure and during CME propagation the mass within that flux rope might be rather constant with variations of about ±25%. The sheath region clearly behaves differently and the geometry most likely deviates from a flux rope shape. We derive only weak correlations between calculated and in-situ measured sheath densities when using different types of volume estimates and the highest correlation is $cc \approx 0.26$ for a reduced rim-like volume structure which is similarly shaped as the CME front. The median differences between calculated and observed sheath densities are larger compared to the magnetic ejecta results and increase when reducing the mass input. This gives indication that the sheath needs to be treated as considerable extra mass.
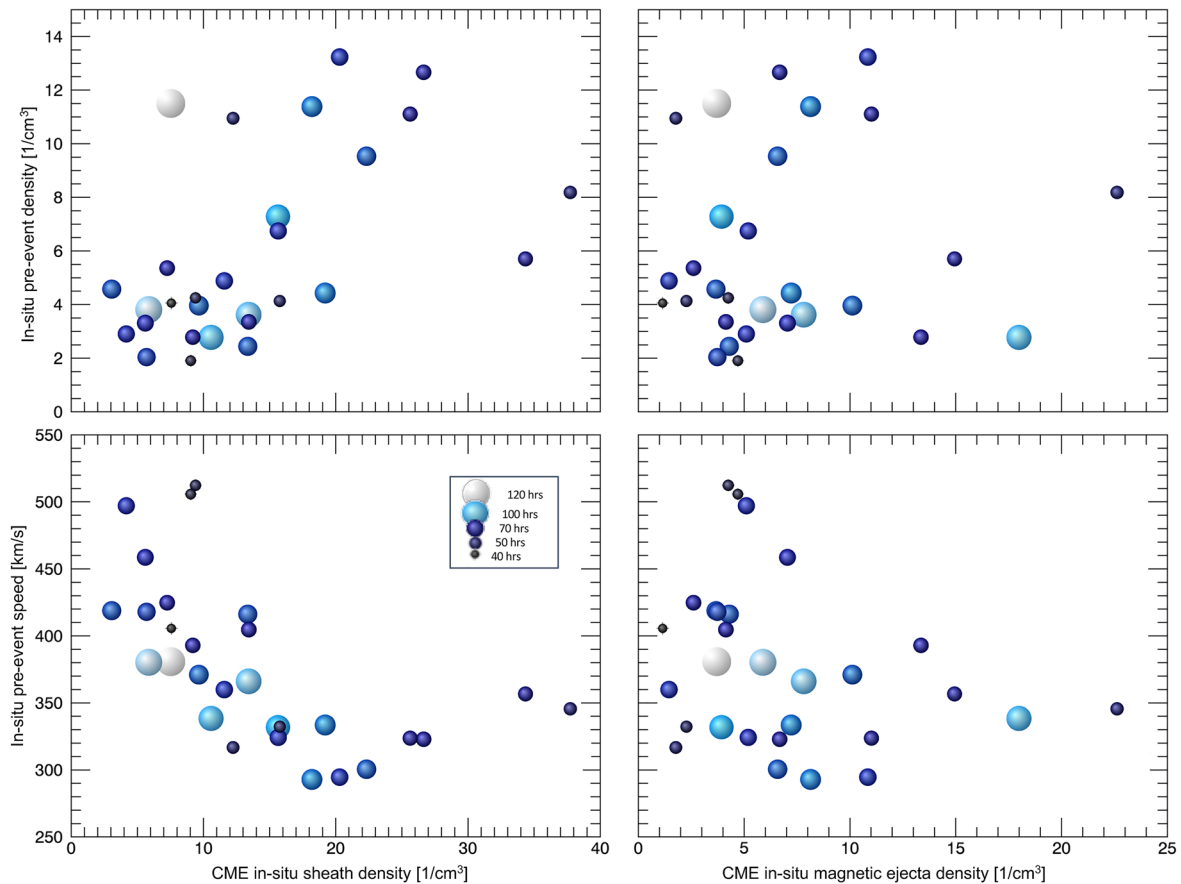
Figure 9. Top: In situ measured solar wind density 24 h before shock arrival versus average density of the sheath (left) and magnetic ejecta (right). Bottom: In situ measured solar wind speed 24 h before shock arrival versus in situ measured average density of the sheath (left) and magnetic ejecta (right). Color coded bubbles mark the propagation duration (transit time) of the CME in hours (see legend).

We find a moderate anti-correlation between the GCS source region longitude and transit time, that is, the more west the source region the shorter the propagation duration (fast CMEs are deflected eastward, slow ones westward; since we observe a plasma pileup, our study covers mainly fast CMEs; see also Sudar et al., 2016; Wang et al., 2004). A weak positive correlation ($cc \approx 0.30$) with the measured density is obtained, hence, the more eastward a CME is launched the higher the in-situ measured density. This might hint toward different levels of compression in dependence of the source region location. However, we note that the CME propagation direction might change in interplanetary space (deflection).

Significant relations are found between in situ measured sheath density and pre-event solar wind conditions (speed and density). Moreover, the geometry of a CME tends to be better related to the measured sheath density than to the ME density. This gives further evidence that the sheath region is largely composed of ambient solar wind material as the CME propagates through interplanetary space. The sheath density is found to be higher when the CME propagates in slow solar wind (cf. top and bottom panel to the left in Figure 9). This could also be interpreted in terms of compression which is larger for CMEs propagating in slow solar wind (Owens, 2018). Slow solar wind is denser compared to fast streams, hence, CMEs propagating in slow solar wind are of higher sheath densities as there is more material ahead of the CME to be piled up.

Our findings are supported by previous studies such as DeForest et al. (2013) who reports a CME mass increase in interplanetary space of the order of 60% and Janvier et al. (2019) who finds for aligned events covering Mercury and Earth measurements, a relative increase of the duration of the sheath compared to the ME structure. Typically, the variation of CME mass as consequence of the interaction with the background solar wind is described by the concept of virtual mass (Cargill, 2004; Cargill et al., 1996). More explicitly, the "snow plow" model considers solar wind mass pile-up at the CME front in analogy to a plow (Tappin, 2006).

Table 3
Spearman Median Correlation Coefficient Derived From the Bootstrapping Analysis for the Pre-event Density Measured Between 24 and 48 h (pre24 and pre48), Respectively, Before Shock Arrival Versus Sheath and ME Density (de), Speed (v) and Total Magnetic Field (B) Taken From In-Situ Measurements

In-situ	pre24-de	pre48-de	pre24-v	pre48-v	pre24-B	pre48-B
sheath-de	0.56	0.50	−0.73	−0.66	0.10	−0.06
(CI 80%)	(0.70; 0.37)	(0.67; 0.30)	(−0.63; −0.80)	(−0.52; −0.77)	(0.33; −0.16)	(0.18; −0.30)
ME-de	0.08	0.09	−0.30	−0.19	−0.18	−0.20
(CI 80%)	(0.30; −0.16)	(0.30; −0.13)	(−0.09; −0.48)	(0.02; −0.40)	(0.06; −0.42)	(0.036; −0.43)

The average CME density ratio with the background solar wind is ∼11 at 15 R_s and ∼6 at 30 R_s (see also Ontiveros & Vourlidas, 2009). For 21.5 R_s (inner boundary for heliospheric models), we obtain a ratio of ∼ 7 ± 4. Keeping in mind that the background solar wind density is based on slow solar wind, our results suggest dcld values higher than the default values currently used for CME propagation models. It is known that variations of the density parameter strongly influence the CME propagation time and impact speed (Mays et al., 2015; Werner et al., 2019). Values derived from observations should be used as cross-check and to restrict the choice of free parameters in the propagation models. In the Appendix A, model input CME parameters for the sample of 29 events are given for the distance range 21.5 R_s.

5. Conclusions

The current study is based on observational data from remote sensing and in-situ instruments combined with GCS fitting. The simple geometry assumptions used and the unknown mass and geometry evolution in interplanetary space, makes it unfeasible to exactly pin down the complex relations between CME expansion, mass evolution and interaction with the solar wind. However, from the statistical analysis we derive specific trends from which we conclude as follows.

CME magnetic structure:

- our results are in agreement with a scenario in which the major part of CME mass close to the Sun, as measured from remote sensing white-light data, lies within a closed magnetic structure (presumably the flux rope)
- during propagation some mass exchange with the ambient solar wind could be possible
  - measured in-situ densities within the magnetic ejecta could be explained by a CME volume expanding self-similarly with $x \approx 0.9 - 1.0$

CME sheath region:

- the sheath region forms and consists of piled-up interplanetary solar wind material
- the amount of piled-up mass depends on (1) the prevailing density and solar wind flow speed in interplanetary space ahead of the CME, and (2) the CME size (wider CMEs act as piston leading to a stronger mass pile-up compared to narrow CMEs acting like a bow shock where plasma can more easily flow around)

With the newly launched satellites Parker Solar Probe (PSP; Fox et al., 2016) and Solar Orbiter (Müller et al., 2020), we will have more information on the CME density for various distances. PSP orbits in the near future will access the LASCO/C3 coronagraphic field of view (<30 R_s) and approach the Sun as close as 10 R_s. With that we will have the opportunity to actually measure CME density characteristics over the distance range 15–30 R_s and to compare with the derived results from this study.

Table 4
Spearman Median Correlation Coefficient Derived From the Bootstrapping Analysis Between GCS Geometry Parameters α (Angular Half-Width), κ (Aspect Ratio) as Defined in Section 2.1, the GCS Source Region Longitude (lon) and Latitude (lat) and CME Parameters From Remote Sensing and In-Situ Data Against Measured Sheath Density (Sheath de) and ME Density (ME de)

GCS parameter	Transit time	m_{dp}	Sheath de	ME de
α	−0.60	0.67	0.19	0.16
(CI 80%)	(−0.42; −0.74)	(0.77; 0.53)	(−0.06; 0.43)	(−0.10; 0.40)
κ	−0.62	0.39	0.30	−0.13
(CI 80%)	(−0.42; −0.76)	(0.58; 0.16)	(0.08; 0.51)	(−0.38; 0.10)
lon	−0.41	0.22	0.30	0.08
(CI 80%)	(−0.59; −0.17)	(−0.03; 0.45)	(0.05; 0.51)	(−0.18; 0.32)
lat	−0.08	0.08	0.11	−0.01
(CI 80%)	(−0.35; −0.22)	(−0.18; 0.32)	(−0.14; 0.36)	(−0.26; 0.24)

Appendix A: CME-ICME Pairs—Event Parameters

Table A1 gives for the 29 CME-ICME pairs under study relevant parameters that may be used as input for modeling. For identification of the CME-ICME pairs we give the CDAW catalog time based on LASCO observations (Yashiro et al., 2004) and the ICME disturbance arrival time according to the R&C list (Richardson & Cane, 2010). We list from GCS reconstructions (based on remote sensing data from two or three different vantage points) the following parameters: longitude, latitude in Stonyhurst coordinates, the tilt as the angle of the flux rope axis with respect to the equatorial plane, and the geometry parameters α and κ from which the volume is calculated (Holzknecht et al., 2018). The deprojected mass is derived at a distance of about 15 R_s using combined STEREO-A and -B COR2 data. For the distance of 21.5 R_s (0.1 AU) we give the CME speed and time (kinematics are derived from GCS reconstructions covering several time steps, and making a linear extrapolation from the last two data points to estimate the values for 21.5 R_s). The density is derived from the deprojected mass divided by the CME volume applying $h = 21.5$ R_s. From in-situ measurements we give the average speed over the sheath region (to estimate the impact speed at 1 AU distance) and the average ME speed, as well as the average sheath and ME particle density. We also list the calculated density based on the reduced CME volume for sheath and ME region applying $x = 0.9$. To feed ensemble CME propagation models, we give general estimates of uncertainties empirically derived from the analysis performed during this study: ± 30 min in timing, ± 50–200 km/s for speed, 10% for α and κ, 30% for the deprojected mass and density, $\pm 10°$ for longitude and latitude, and $\pm 20°$ in tilt.

Table A1
Parameters Derived for Each of the CME Events Under Study (No.) Including a Flag (q) Marking the GCS Fit as Very Easy (1), Easy (2), and Hard (3) to Perform

no.(q)	LASCO	Lon	Lat	Tilt	α	κ	m_{dp}	By	Time	v	ρ	Disturbance	$\overline{v}_{sh}$	$\overline{v}_{ME}$	$\overline{n}_{p\,sh}$	$\overline{n}_{p\,ME}$	$\overline{n}_{p\,sh}$	$\overline{n}_{p\,ME}$
				Remote sensing of the Sun and GCS results					21.5R_s (0.1 AU)			In situ measurements at 215R_s (1 AU)			Calculated			
1 (3)	2008/12/12 0525	4	5	51	0.23	0.27	4.50E15	HC	2008/12/12 1500	470	1.36E-17	2008/12/16 0800	350	340	15.7	3.9	22.8	11.3
2 (3)	2009/12/16 0430	−2	7	−6	0.39	0.31	2.20E15	HC	2009/12/16 1230	370	4.81E-18	2009/12/19 1000	430	380	3.0	3.7	5.8	3.8
3 (2)	2010/04/03 1033	3	−29	2	0.42	0.29	6.04E15	UG	2010/04/03 1350	900	1.42E-17	2010/04/05 0826	720	650	9.4	4.2	9.0	5.9
4 (2)	2010/04/08 0454	−2	−9	−29	0.57	0.19	7.52E15	NS	2010/04/08 0900	500	3.08E-17	2010/04/11 1304	430	410	9.7	10.1	39.9	28.3
5 (2)	2010/05/24 1406	13	8	−10	0.24	0.48	3.20E15	HC	2010/05/24 0240	390	4.36E-18	2010/05/28 0258	370	360	19.2	7.2	4.3	2.8
6 (1)	2010/06/16 0635	−17	3	−33	0.17	0.26	2.35E15	NS	2010/06/16 2330	430	7.97E-18	2010/06/20 2000	390	360	5.9	5.9	9.3	3.8
7 (3)	2010/10/26 0200	18	−25	−55	0.52	0.26	7.14E15	NS	2010/10/26 1730	450	1.86E-17	2010/10/30 1015	380	340	13.4	7.8	10.4	7.2
8 (3)	2011/01/30 2008	−40	−12	−20	0.20	0.26	5.60E15	HC	2011/01/30 2150	310	1.84E-17	2011/02/04 0155	370	410	10.6	18.0	56.3	25.8
9 (2)	2011/02/15 0236	0	−11	53	0.37	0.46	6.83E15	UG	2011/02/15 0630	700	8.95E-18	2011/02/18 0130	540	470	11.6	1.4	3.4	2.4
10 (1)	2011/03/03 0548	8	−23	8	0.38	0.35	3.13E15	NS	2011/03/03 1300	510	5.83E-18	2011/03/06 0331	530	440	4.2	5.1	3.0	2.0
11 (3)	2011/06/02 0745	42	12	55	0.42	0.40	3.80E15	HC	2011/06/02 1100	830	5.78E-18	2011/06/04 2045	480	510	34.3	14.9	7.2	5.1
12 (1)	2011/06/14 0610	−44	−1	41	1.00	0.28	1.03E16	NS	2011/06/14 1300	770	2.14E-17	2011/06/17 0241	530	490	5.6	7.0	57.3	51.5
13 (1)	2011/08/04 0412	31	20	62	0.87	0.49	6.84E15	UG	2011/08/04 0550	1300	6.93E-18	2011/08/05 1751	540	540	7.5	1.2	2.1	1.9

no.(q)			Remote sensing of the Sun and GCS results					21.5R$_s$ (0.1 AU)				In situ measurements at 215R$_s$ (1 AU)			Calculated			
	LASCO	Lon	Lat	Tilt	α	κ	m_{dp}	By	Time	v	ρ	Disturbance	$\overline{v}_{sh}$	$\overline{v}_{ME}$	$\overline{n}_{p\,sh}$	$\overline{n}_{p\,ME}$	$\overline{n}_{p\,sh}$	$\overline{n}_{p\,ME}$
14 (1)	2011/09/13 2210	19	21	−6	0.22	0.47	4.20E15	HC	2011/09/14 0620	600	5.98E-18	2011/09/17 0343	500	450	13.3	4.3	7.1	4.4
15 (1)	2011/10/22 0005	87	45	16	0.79	0.59	1.23E16	NS	2011/10/22 1330	610	1.01E-17	2011/10/24 1831	480	470	25.6	11.0	12.2	11.0
16 (2)	2011/10/27 1200	−37	29	17	0.29	0.36	3.01E15	NS	2011/10/27 1550	700	5.76E-18	2011/11/01 0907	400	370	7.5	3.7	4.8	2.9
17 (1)	2011/11/26 0700	56	14	−41	0.77	0.63	1.00E16	HC	2011/11/26 1000	1350	7.67E-18	2011/11/28 2150	500	450	9.2	13.4	22.3	20.1
18 (1)	2012/01/19 1512	−20	44	90	1.00	0.47	9.17E15	NS	2012/01/19 1730	1000	9.60E-18	2012/01/22 0611	410	450	26.6	6.7	10.9	10.0
19 (2)	2012/03/13 1736	62	21	−40	1.28	0.74	1.00E16	NS	2012/03/13 1940	850	6.02E-18	2012/03/15 1306	710	710	9.1	4.7	4.3	4.3
20 (2)	2012/06/14 1412	1	−24	67	0.65	0.52	8.46E15	UG	2012/06/14 1700	1000	8.39E-18	2012/06/16 2019	490	450	37.7	22.6	15.7	13.2
21 (2)	2012/07/12 1648	7	−18	70	0.39	0.59	1.84E16	UG	2012/07/12 1900	1150	1.75E-17	2012/07/14 1809	610	490	15.8	2.3	5.2	4.1
22 (2)	2012/09/28 0000	11	10	75	0.60	0.40	9.61E15	UG	2012/09/28 0300	1000	1.34E-17	2012/09/30 2305	370	370	20.3	10.8	19.8	15.5
23 (1)	2012/10/05 0724	21	−18	41	0.57	0.40	6.40E15	UG	2012/10/05 0900	600	9.05E-18	2012/10/08 0516	370	400	15.7	5.2	8.3	6.4
24 (2)	2012/11/09 1512	−11	−18	6	0.60	0.48	5.19E15	NS	2012/11/09 1900	600	5.77E-18	2012/11/12 2204	410	380	22.3	6.5	6.5	5.2
25 (1)	2012/11/23 1336	−22	−21	−66	0.18	0.56	3.45E15	NS	2012/11/23 1810	680	4.06E-18	2012/11/26 0512	520	450	7.3	2.6	2.1	1.4
26 (1)	2013/04/11 0724	−16	−3	41	0.52	0.40	1.51E16	UG	2013/04/11 1130	700	2.18E-17	2013/04/13 2254	490	410	13.4	4.1	11.2	8.3
27 (2)	2013/07/09 1512	0	2	1	0.50	0.38	2.93E15	UG	2013/07/09 2150	550	4.57E-18	2013/07/12 1714	480	410	5.7	3.7	2.1	1.5
28 (1)	2013/09/29 2145	24	23	90	0.82	0.43	1.37E16	NS	2013/09/30 0100	1000	1.65E-17	2013/10/02 0154	590	470	12.2	1.8	6.9	5.9
29 (2)	2014/08/15 1812	15	13	−65	0.38	0.30	1.60E15	UG	2014/08/16 0140	450	3.68E-18	2014/08/19 0657	370	360	18.2	8.1	2.9	1.8

Notes. We give the CDAW catalog observation time, GCS reconstruction parameters lon(gitude) [°], lat(itude) [°], tilt [°], α (rad), and κ (rad), the deprojected mass m_{dp} [g], and information by whom the information was provided (HC, HELCATS; NS, Nishtha Sachdeva; UG, UNIGRAZ). For the distance of 21.5 R$_s$, we give the extrapolated CME speed and time, and the calculated mass density (kg/m^3). From in-situ measurements, we list the ICME disturbance arrival time according to the R&C list (Richardson & Cane, 2010), the average sheath and ME speed (km/s), the average proton number density for sheath and ME. The last two columns give the calculated proton number density based on the reduced CME volume applying $x = 0.9$.

Data Availability Statement

References

Bein, B. M., Temmer, M., Vourlidas, A., Veronig, A. M., & Utz, D. (2013). The height evolution of the "True" coronal mass ejection mass derived from STEREO COR1 and COR2 observations. *The Astrophysical Journal*, *768*(1), 31. https://doi.org/10.1088/0004-637X/768/1/31

Bemporad, A., & Mancuso, S. (2010). First complete determination of plasma physical parameters across a coronal mass ejection-driven hock. *The Astrophysical Journal*, *720*(1), 130–143. https://doi.org/10.1088/0004-637X/720/1/130

Bothmer, V., & Schwenn, R. (1998). The structure and origin of magnetic clouds in the solar wind. *Annales Geophysicae*, *16*, 1–24. https://doi.org/10.1007/s00585-997-0001-x

Cargill, P. J. (2004). On the aerodynamic drag force acting on interplanetary coronal mass ejections. *Solar Physics*, *221*, 135–149. https://doi.org/10.1023/B:SOLA.0000033366.10725.a2

Cargill, P. J., Chen, J., Spicer, D. S., & Zalesak, S. T. (1996). Magnetohydrodynamic simulations of the motion of magnetic flux tubes through a magnetized plasma. *Journal of Geophysical Research*, *101*, 4855–4870. https://doi.org/10.1029/95JA03769

Chen, J. (1989). Effects of toroidal forces in current loops embedded in a background plasma. *The Astrophysical Journal*, *338*, 453–470. https://doi.org/10.1086/167211

Chen, J. (1996). Theory of prominence eruption and propagation: Interplanetary consequences. *Journal of Geophysical Research*, *101*, 27499–27520. https://doi.org/10.1029/96JA02644

Colaninno, R. C., & Vourlidas, A. (2009). First determination of the true mass of coronal mass ejections: A novel approach to using the Two STEREO viewpoints. *The Astrophysical Journal*, *698*(1), 852–858. https://doi.org/10.1088/0004-637X/698/1/852

Dasso, S., Nakwacki, M. S., Démoulin, P., & Mand rini, C. H. (2007). Progressive transformation of a flux rope to an ICME. Comparative analysis using the direct and fitted expansion methods. *Solar Physics*, *244*(1–2), 115–137. https://doi.org/10.1007/s11207-007-9034-2

DeForest, C. E., Howard, T. A., & McComas, D. J. (2013). Tracking coronal features from the low corona to Earth: A quantitative analysis of the 2008 December 12 coronal mass ejection. *The Astrophysical Journal*, *769*(1), 43. https://doi.org/10.1088/0004-637X/769/1/43

Démoulin, P., Nakwacki, M. S., Dasso, S., & Mandrini, C. H. (2008). Expected in Situ velocities from a hierarchical model for expanding interplanetary coronal mass ejections. *Solar Physics*, *250*, 347–374. https://doi.org/10.1007/s11207-008-9221-9

Domingo, V., Fleck, B., & Poland, A. I. (1995). The SOHO Mission: An overview. *Solar Physics*, *162*, 1–37. https://doi.org/10.1007/BF00733425

Dumbović, M., Čalogović, J., Vršnak, B., Temmer, M., Mays, M. L., Veronig, A., & Piantschitsch, I. (2018). The drag-based ensemble model (DBEM) for coronal mass ejection propagation. *The Astrophysical Journal*, *854*(2), 180. https://doi.org/10.3847/1538-4357/aaaa66

Dumbović, M., Guo, J., Temmer, M., Mays, M. L., Veronig, A., Heinemann, S. G., et al. (2019). Unusual plasma and particle signatures at Mars and STEREO-A related to CME-CME interaction. *The Astrophysical Journal*, *880*(1), 18. https://doi.org/10.3847/1538-4357/ab27ca

Efron, B. (1979). Bootstrap methods: Another look at the jackknife. *Annals of Statistics*, *7*(1), 1–26. Retrieved from https://doi.org/10.1214/aos/1176344552

Efron, B., & Tibshirani, R. J. (1993). *An introduction to the bootstrap*. New York, NY: Chapman & Hall.

Fox, N. J., Velli, M. C., Bale, S. D., Decker, R., Driesman, A., Howard, R. A., et al. (2016). The solar probe plus mission: Humanity's first visit to our star. *Space Science Reviews*, *204*(1–4), 7–48. https://doi.org/10.1007/s11214-015-0211-6

Gonzalez, W. D., Tsurutani, B. T., Gonzalez, A. L. C., Smith, E. J., Tang, F., & Akasofu, S.-I. (1989). Solar wind-magnetosphere coupling during intense magnetic storms (1978-1979). *Journal of Geophysical Research*, *94*(A7), 8835–8851. https://doi.org/10.1029/JA094iA07p08835

Gulisano, A. M., Démoulin, P., Dasso, S., & Rodriguez, L. (2012). Expansion of magnetic clouds in the outer heliosphere. *Astronomy & Astrophysics*, *543*, A107. https://doi.org/10.1051/0004-6361/201118748

Hill, F., Martens, P., Yoshimura, K., Gurman, J., Hourclé, J., Dimitoglou, G., et al. (2009). The virtual solar observatory—A resource for international heliophysics research. *Earth, Moon, and Planets*, *104*(1–4), 315–330. https://doi.org/10.1007/s11038-008-9274-7

Holzknecht, L., Temmer, M., Dumbović, M., Wellenzohn, S., Krikova, K., Heinemann, S. G., et al. (2018). CME volume calculation from 3D GCS reconstruction. *Central European Astrophysical Bulletin*, *42*, 3.

Howard, R. A., Moses, J. D., Vourlidas, A., Newmark, J. S., Socker, D. G., Plunkett, S. P., et al. (2008). Sun Earth connection coronal and heliospheric investigation (SECCHI). *Space Science Reviews*, *136*, 67–115. https://doi.org/10.1007/s11214-008-9341-4

Howard, R. A., & Vourlidas, A. (2018). Evolution of CME Mass in the corona. *Solar Physics*, *293*(4), 55. https://doi.org/10.1007/s11207-018-1274-9

Janvier, M., Winslow, R. M., Good, S., Bonhomme, E., Démoulin, P., Dasso, S., et al. (2019). Generic magnetic field intensity profiles of interplanetary coronal mass ejections at Mercury, Venus, and Earth from superposed epoch analyses. *Journal of Geophysical Research (Space Physics)*, *124*(2), 812–836. https://doi.org/10.1029/2018JA025949

Kaiser, M. L., Kucera, T. A., Davila, J. M., St Cyr, O. C., Guhathakurta, M., & Christian, E. (2008). The STEREO mission: An introduction. *Space Science Reviews*, *136*(1–4), 5–16. https://doi.org/10.1007/s11214-007-9277-0

Kilpua, E., Koskinen, H. E. J., & Pulkkinen, T. I. (2017). Coronal mass ejections and their sheath regions in interplanetary space. *Living Reviews in Solar Physics*, *14*(1), 5. https://doi.org/10.1007/s41116-017-0009-6

Kliem, B., & Török, T. (2006). Torus instability. *Physical Review Letters*, *96*(25), 255002. https://doi.org/10.1103/PhysRevLett.96.255002

Leblanc, Y., Dulk, G. A., & Bougeret, J.-L. (1998). Tracing the electron density from the corona to 1au. *Solar Physics*, *183*(1), 165–180. https://doi.org/10.1023/A:1005049730506

Leitner, M., Farrugia, C. J., MöStl, C., Ogilvie, K. W., Galvin, A. B., Schwenn, R., & Biernat, H. K. (2007). Consequences of the force-free model of magnetic clouds for their heliospheric evolution. *Journal of Geophysical Research*, *112*, A06113. https://doi.org/10.1029/2006JA011940

Lepping, R. P., Acūna, M. H., Burlaga, L. F., Farrell, W. M., Slavin, J. A., Schatten, K. H., et al. (1995). The wind magnetic field investigation. *Space Science Reviews*, *71*(1–4), 207–229. https://doi.org/10.1007/BF00751330

Manchester, W. B., Kozyra, J. U., Lepri, S. T., & Lavraud, B. (2014). Simulation of magnetic cloud erosion during propagation. *Journal of Geophysical Research (Space Physics)*, *119*(7), 5449–5464. https://doi.org/10.1002/2014JA019882

Masías-Meza, J. J., Dasso, S., Démoulin, P., Rodriguez, L., & Janvier, M. (2016). Superposed epoch study of ICME sub-structures near Earth and their effects on Galactic cosmic rays. *Astronomy & Astrophysics*, *592*, A118. https://doi.org/10.1051/0004-6361/201628571

Mays, M. L., Taktakishvili, A., Pulkkinen, A., MacNeice, P. J., Rastätter, L., Odstrcil, D., et al. (2015). Ensemble modeling of CMEs using the WSA-ENLIL+ Cone model. *Solar Physics*, *290*(6), 1775–1814. https://doi.org/10.1007/s11207-015-0692-1

Müller, D., Zouganelis, I., Cyr, StO. C., Gilbert, H. R., & Nieves-Chinchilla, T. (2020). Europe's next mission to the Sun. *Nature Astronomy*, *4*, 205. https://doi.org/10.1038/s41550-020-1015-5

Odstrčil, D., & Pizzo, V. J. (1999). Three-dimensional propagation of CMEs in a structured solar wind flow: 1. CME launched within the streamer belt. *Journal of Geophysical Research*, *104*, 483–492. https://doi.org/10.1029/1998JA900019

Ogilvie, K. W., Chornay, D. J., Fritzenreiter, R. J., Hunsaker, F., Keller, J., Lobell, J., et al. (1995). SWE, A comprehensive plasma instrument for the wind spacecraft. *Space Science Reviews*, *71*(1–4), 55–77. https://doi.org/10.1007/BF00751326

Ontiveros, V., & Vourlidas, A. (2009). Quantitative measurements of coronal mass ejection-driven shocks from LASCO observations. *The Astrophysical Journal*, *693*(1), 267–275. https://doi.org/10.1088/0004-637X/693/1/267

Owens, M. J. (2018). Solar wind and heavy ion properties of interplanetary coronal mass ejections. *Solar Physics*, *293*(8), 122. Retrieved from https://doi.org/10.1007/s11207-018-1343-0

Pluta, A., Mrotzek, N., Vourlidas, A., Bothmer, V., & Savani, N. (2019). Combined geometrical modeling and white-light mass determination of coronal mass ejections. *Astronomy and Astrophysics*, *623*, A139. https://doi.org/10.1051/0004-6361/201833829

Pomoell, J., & Poedts, S. (2018). EUHFORIA: European heliospheric forecasting information asset. *Journal of Space Weather and Space Climate*, *8*, A35. https://doi.org/10.1051/swsc/2018020

Richardson, I. G., & Cane, H. V. (2010Jun 01). Near-earth interplanetary coronal mass ejections during solar cycle 23 (1996–2009): Catalog and summary of properties. *Solar Physics*, *264*(1), 189–237.Retrieved from https://doi.org/10.1007/s11207-010-9568-6

Riley, P., Mays, M. L., Andries, J., Amerstorfer, T., Biesecker, D., Delouille, V., et al. (2018). Forecasting the arrival time of coronal mass ejections: Analysis of the CCMC CME Scoreboard. *Space Weather*, *16*(9), 1245–1260. https://doi.org/10.1029/2018SW001962

Rouillard, A. P. (2011). Relating white light and in situ observations of coronal mass ejections: A review. *Journal of Atmospheric and Solar: Terrestrial Physics*, *73*(10), 1201–1213. https://doi.org/10.1016/j.jastp.2010.08.015

Ruffenach, A., Lavraud, B., Farrugia, C. J., Démoulin, P., Dasso, S., Owens, M. J., et al. (2015). Statistical study of magnetic cloud erosion by magnetic reconnection. *Journal of Geophysical Research (Space Physics)*, *120*(1), 43–60. https://doi.org/10.1002/2014JA020628

Sachdeva, N. (2019). *Dynamics of solar coronal mass ejections: Forces that impact their propagation (PhD thesis archive)*. Academic Framework of the PhD Program at IISER Pune, Pune, India.

Sachdeva, N., Subramanian, P., Colaninno, R., & Vourlidas, A. (2015). CME Propagation: Where does aerodynamic drag 'Take Over'? *The Astrophysical Journal*, *809*(2), 158. https://doi.org/10.1088/0004-637X/809/2/158

Savani, N. P., Vourlidas, A., Pulkkinen, A., Nieves-Chinchilla, T., Lavraud, B., & Owens, M. J. (2013). Tracking the momentum flux of a CME and quantifying its influence on geomagnetically induced currents at Earth. *Space Weather*, *11*(5), 245–261. https://doi.org/10.1002/swe.20038

Siscoe, G., & Odstrcil, D. (2008). Ways in which ICME sheaths differ from magnetosheaths. *Journal of Geophysical Research*, *113*(A9), A00B07. https://doi.org/10.1029/2008JA013142

Sudar, D., Vršnak, B., & Dumbović, M. (2016). Predicting coronal mass ejections transit times to Earth with neural network. *MNRAS* , *456*(2), 1542–1548. https://doi.org/10.1093/mnras/stv2782

Takahashi, T., & Shibata, K. (2017). Sheath-accumulating propagation of interplanetary coronal mass ejection. *The Astrophysical Journal*, *837*(2), L17. https://doi.org/10.3847/2041-8213/aa624c

Tappin, S. J. (2006). The deceleration of an interplanetary transient from the Sun to 5 Au. *Solar Physics*, *233*(2), 233–248. https://doi.org/10.1007/s11207-006-2065-2

Temmer, M., Reiss, M. A., Nikolic, L., Hofmeister, S. J., & Veronig, A. M. (2017). Preconditioning of interplanetary space due to transient CME disturbances. *The Astrophysical Journal*, *835*(2), 141. https://doi.org/10.3847/1538-4357/835/2/141

Temmer, M., Rollett, T., Möstl, C., Veronig, A. M., Vršnak, B., & Odstrčil, D. (2011). Influence of the ambient solar wind flow on the propagation behavior of interplanetary coronal mass ejections. *The Astrophysical Journal*, *743*(2), 101. https://doi.org/10.1088/0004-637X/743/2/101

Thernisien, A. (2011). Implementation of the graduated cylindrical shell model for the three-dimensional reconstruction of coronal mass ejections. *The Astrophysical Journal*, *194*, 33. https://doi.org/10.1088/0067-0049/194/2/33

Thernisien, A., Vourlidas, A., & Howard, R. A. (2009). Forward modeling of coronal mass ejections using STEREO/SECCHI data. *Solar Physics*, *256*, 111–130. https://doi.org/10.1007/s11207-009-9346-5

Veronig, A. M., Gömöry, P., Dissauer, K., Temmer, M., & Vanninathan, K. (2019). Spectroscopy and differential emission measure diagnostics of a coronal dimming associated with a Fast Halo CME. *The Astrophysical Journal*, *879*(2), 85. https://doi.org/10.3847/1538-4357/ab2712

Vršnak, B. (2001). Dynamics of solar coronal eruptions. *Journal of Geophysical Research*, *106*, 25249–25260. https://doi.org/10.1029/2000JA004007

Vršnak, B. (2008). Processes and mechanisms governing the initiation and propagation of CMEs. *Annales Geophysicae*, *26*(10), 3089–3101. https://doi.org/10.5194/angeo-26-3089-2008

Vršnak, B. (2016). Solar eruptions: The CME-flare relationship. *Astronomische Nachrichten*, *337*(10), 1002. https://doi.org/10.1002/asna.201612424

Vršnak, B., Amerstorfer, T., Dumbović, M., Leitner, M., Veronig, A. M., Temmer, M., et al. (2019). Heliospheric evolution of magnetic clouds. *The Astrophysical Journal*, *877*(2), 77. https://doi.org/10.3847/1538-4357/ab190a

Vršnak, B., Vrbanec, D., & Čalogović, J. (2008). Dynamics of coronal mass ejections. The mass-scaling of the aerodynamic drag. *Astronomy & Astrophysics*, *490*, 811–815. https://doi.org/10.1051/0004-6361:200810215

Vršnak, B., Žic, T., Falkenberg, T. V., Möstl, C., Vennerstrom, S., & Vrbanec, D. (2010). The role of aerodynamic drag in propagation of interplanetary coronal mass ejections. *Astronomy & Astrophysics*, *512*, A43. https://doi.org/10.1051/0004-6361/200913482

Vršnak, B., Žic, T., Vrbanec, D., Temmer, M., Rollett, T., Möstl, C., et al. (2013). Propagation of interplanetary coronal mass ejections: The drag-based model. *Solar Physics*, *285*(1–2), 295–315. https://doi.org/10.1007/s11207-012-0035-4

Wang, Y., Shen, C., Wang, S., & Ye, P. (2004). Deflection of coronal mass ejection in the interplanetary medium. *Solar Physics*, *222*(2), 329–343. https://doi.org/10.1023/B:SOLA.0000043576.21942.aa

Werner, A. L. E., Yordanova, E., Dimmock, A. P., & Temmer, M. (2019). Modeling the multiple CME interaction event on 6-9 September 2017 with WSA-ENLIL+ Cone. *Space Weather*, *17*(2), 357–369. https://doi.org/10.1029/2018SW001993

Wood, B. E., Wu, C.-C., Lepping, R. P., Nieves-Chinchilla, T., Howard, R. A., Linton, M. G., & Socker, D. G. (2017). A STEREO survey of magnetic cloud coronal mass ejections observed at Earth in 2008-2012. *The Astrophysical Journal*, *229*(2), 29. https://doi.org/10.3847/1538-4365/229/2/29

Yashiro, S., Gopalswamy, N., Michalek, G., St Cyr, O. C., Plunkett, S. P., Rich, N. B., & Howard, R. A. (2004). A catalog of white light coronal mass ejections observed by the SOHO spacecraft. *Journal of Geophysical Research*, *109*(A7), A07105. https://doi.org/10.1029/2003JA010282